frontiers | Frontiers in Nuclear Engineering

TYPE Original Research
PUBLISHED 15 October 2024
DOI 10.3389/fnuen.2024.1465080

OPEN ACCESS

EDITED BY
Thierry Wiss,
Joint Research Centre, Germany

REVIEWED BY
Romain Vauchy,
Japan Atomic Energy Agency, Japan
Lionel Desgranges,
Commissariat à l'Energie Atomique et aux Energies Alternatives (CEA), France

*CORRESPONDENCE
C. Gaillard,
gaillard@ipnl.in2p3.fr

RECEIVED 15 July 2024
ACCEPTED 16 September 2024
PUBLISHED 15 October 2024

CITATION
Gaillard C, Lotz H, Sarrasin L, Pipon Y, Ducher R and Moncoffre N (2024) Insights into the UO_{2+x}/U_4O_9 phase characterization in oxidized UO_2 pellets as a function of hyper-stoichiometry.
Front. Nucl. Eng. 3:1465080.
doi: 10.3389/fnuen.2024.1465080

Insights into the UO_{2+x}/U_4O_9 phase characterization in oxidized UO_2 pellets as a function of hyper-stoichiometry

C. Gaillard[1]*, H. Lotz[1], L. Sarrasin[1], Y. Pipon[1,2], R. Ducher[3] and N. Moncoffre[1]

[1]University Lyon, University Claude Bernard Lyon 1, CNRS/IN2P3, IP2I Lyon, Villeurbanne, France, [2]University Lyon, University Claude Bernard Lyon 1, IUT Lyon-1, Département Chimie, Lyon, France, [3]IRSN, LETR—BP3, St-Paul-Lez-Durance Cedex, France

We present new insights into the study of the UO_{2+x}/U_4O_9 equilibrium in UO_2 as a function of the hyper-stoichiometry (x) by coupling HERFD-XANES at the uranium M_4-edge with micro-Raman spectroscopy mapping. XANES allowed the measurement of uranium speciation in the samples, while Raman spectroscopy was used to individually characterize the composition and localization of the different oxide phases. UO_2 pellets were oxidized under dry conditions at temperatures above the UO_{2+x}/U_4O_9 phase transition to reach hyper-stoichiometries in the range of $0.01 \leq x \leq 0.1$. Combining both techniques, we could determine the proportions of U_4O_9 and UO_{2+x}. We show that at a low O/U ratio, U_4O_9 is present as small clusters inside UO_2 grains. As the O/U increases, we found evidence of the formation of a network of U_4O_9 crystallized inside the UO_{2+x} grains. The variation of the UO_{2+x} phase hyper-stoichiometry (x) was evaluated as a function of the sample oxidation.

KEYWORDS

UO_2, oxidation, U_4O_9, Raman spectroscopy, HERFD-XANES

1 Introduction

Uranium oxide UO_2 is widely studied because of its use as a nuclear fuel in nuclear pressurized water reactor power plants. An important parameter that can affect the fuel's performance is fuel oxidation, which can occur during normal reactor operations in the case of a defective rod or during reactor accident conditions. Under LOCA (LOss of Coolant Accident) conditions, fuel oxidizes due to high temperatures and the steam environment, affecting its thermal properties and the release of fission products (Horlait et al., 2023; Kudo et al., 2007; Le Gall et al., 2020). Understanding oxidation mechanisms and characterizing formed oxide phases are therefore important to evaluate all consequences of this type of accident. Both the kinetics of oxidation and the crystallographic structures of the U–O oxide phases (α, β, γ- U_4O_9, U_3O_7, α, β- U_3O_8) have been studied extensively (Taylor, 2005; Mc Eachern and Taylor, 1998; Rousseau et al., 2006; Desgranges et al., 2011; Garrido et al., 2006; Soulié et al., 2019; Mc Eachern, 1997). UO_2 has a fluorite structure of Fm-3m. At high temperatures, UO_2 oxidation forms a UO_{2+x} single phase, where oxygen atoms are incorporated into the fluorite structure in interstitial octahedral sites. At lower temperatures, UO_{2+x} coexists with α-U_4O_9 (=$UO_{2.25}$). In hyper-stoichiometric compounds, the charge balance is made by the valence change of uranium cations from

U^{4+} to U^{5+}, while interstitial oxygen atoms are accommodated as Willis clusters involving two oxygen vacancies, two oxygen O′ atoms, and two O″ atoms. A further increase in interstitial oxygen atoms leads to a distortion of the unit cell from cubic to tetragonal and ultimately to a monoclinic structure. The formation of U_4O_9 (and U_3O_7) involves a slight volume reduction, while the formation of U_3O_8 involves a 36% volume increase.

The transition mechanism from UO_{2+x} to U_4O_9 has been widely investigated in terms of phase transition, establishing the U–O equilibrium phase diagram (Bannister and Buykx, 1974; Blackburn, 1958; Gronvold, 1955; Guéneau et al., 2002; Higgs et al., 2007; Ishii et al., 1970; Lierde et al., 1970; Matsui and Naito, 1975). However, few have studied the morphological changes in polycrystalline UO_2 after oxidative treatments. Whillock and Pearce studied the distribution and percentage of U_4O_9 in oxidized UO_2 (total O/U ratio between 2.05 and 2.12) (Whillock and Pearce, 1990). They found different types of morphology for U_4O_9 in UO_2, from needles to starbursts or massive blocks, as the U_4O_9 proportion varies from 20% to 40%. Schaner studied the UO_2–U_4O_9 equilibrium phase diagram between $UO_{2.006}$ and $UO_{2.176}$ on polycrystalline UO_2 pellets using metallographic techniques (Schaner, 1960), finding that U_4O_9 solubility in UO_{2+x} depends on temperature. In addition, photomicrographs of the sample surfaces taken after different oxidative treatments at 900 °C show that the U_4O_9 morphology inside UO_{2+x} grains depends on the O/U ratio and on the experimental procedure used to cool the samples at ambient temperature (slow temperature decrease or quenching below the phase transition limit).

In this study, we contribute to the study of the UO_{2+x}/U_4O_9 equilibrium in UO_2 as a function of hyper-stoichiometry by coupling HERFD-XANES at the uranium M_4-edge with micro-Raman spectroscopy mapping. XANES allows the measurement of uranium speciation in the samples, while Raman spectroscopy individually characterizes the composition and localization of the different oxide phases in UO_2 pellets. Combining both techniques, we could determine the proportion between U_4O_9 and UO_{2+x} and evaluate the variation of the UO_{2+x} phase stoichiometry (x) as a function of the sample oxidation.

2 Materials and methods

2.1 Sample preparation

Depleted UO_2 pellets (diameter 9 mm × 1.6 mm thick) of high bulk density (97.5% of the theoretical density) sintered at 1750 °C under reducing conditions (Ar/H_2 5%) for 5 h were provided by Framatome. Their average grain size was 11 μm, which is comparable to that of the PWR nuclear fuel. The pellets were polished on one side by the PRIMEVerre company (Montpellier, France) with a ¼ μm diamond paste. The samples were then annealed in a PECKLY© tubular furnace at 1000 °C for 10 h under vacuum (10^{-7} mbar) to de-gas adsorbed species on the pellets. Second, annealing at 1600 °C for 4 h in a NABERTHERM© tubular furnace was performed under a Ar/H_2 5% gas mixture flowing through ultrahigh capacity oxygen and moisture traps. This thermal treatment allowed annealing of the polishing defects while avoiding UO_2 oxidation.

UO_2 oxidation was performed by thermal annealing under a dry atmosphere using different protocols according to the samples (Table 1). Before and after each annealing, the pellets were weighted with a Sartorius μ-balance with a ±2 μg accuracy. The O/U ratio was calculated from the mass gain of the samples during annealing, with an error of ±0.001.

Samples *UO2_ox1_A* and *UO2_ox1_B* correspond to the same initial pellet. For *UO2_ox1_A*, the pellet was annealed in a NABERTHERM© tubular furnace at 1600 °C under an Ar/O_2 5 ppm gas flow over 4 h, with a ramping of 300°/h for heating and cooling. After annealing, the pellet was weighed and analyzed by Raman spectroscopy. It was then oxidized a second time following the same experimental protocol (sample *UO2_ox1_B*) to reach a final O/U ratio of 2.010. The sample *UO2_ox2* was submitted to the same annealing treatment as *UO2_ox1_B* to reach a 2.010 stoichiometry. Then, it was annealed in a steel tubular furnace at 900 °C for an hour under an Ar/O_2 5 ppm gas flow. According to the O/U phase diagram (Guéneau et al., 2002; Lindemer and Besmann, 1985), this annealing condition allows the dissolution of any U_4O_9 phase that might be present in the sample to form the sole UO_{2+x} phase. Sample quenching was then performed to keep this UO_{2+x} phase at an ambient temperature. This rapid sample cooling, from 900 °C to room temperature, was achieved in 10 minutes under the same atmospheric conditions as those during the annealing (Ar/O_2 5 ppm gas flow). After this quenching, no mass variation was detected on the pellet, so we can assume that its final stoichiometry was the same as before quenching (2.010). Sample *UO2_ox3* was prepared by annealing at 1600 °C under an Ar/O_2 5 ppm gas flow for 15 h. Sample *UO2_ox4* was obtained using a SETARAM© thermobalance. The UO_2 pellet was placed in a quartz boat suspended in an oven. The analyzer was placed in a vacuum for 30 min and then filled with a carrier gas to avoid any gaseous pollution. The gases used were He and Ar/O_2 100 ppm, the introduction of O_2 being controlled by an oxygen sensor. In order to reach the O/U ratio = 2.10, oxidation was performed at 850 °C. A ramp of 10°C.min^{-1} was programmed up to 850 °C, then plateaued at 850 °C until the mass gain was reached, and finally the heating was switched off. O_2 was added only during the plateau at 850 °C, while the increase and decrease in temperature were performed under He. The mass gain was achieved in 3.5 h. Supplementary Figure S1 displays the mass gain variation with time and temperature; these curves show that the mass gain of the pellet is linear with time at 850 °C. The change of atmosphere at the end of the plateau combined with the decrease of temperature (approximately 30 °C/min) probably limited the oxidation to a negligible level during the cooling stage.

2.2 HERFD-XANES measurements at the U M_4-edge

High Energy Resolution Fluorescence Detected XANES (HERFD-XANES) data were measured at the MARS beamline of the SOLEIL synchrotron (Saint-Aubin, France) (Sitaud et al., 2012) on pellets. Spectra were measured at room temperature at the U M_4-edge (3728 eV) using a double-crystal monochromator (DCM) equipped with a pair of Si(111) crystals. Higher harmonic rejection and vertical focusing were achieved using the Si strip of

TABLE 1 Summary of the sample oxidative treatments.

Sample ID	O/U ratio	Sample oxidative treatment
UO_2	2.000	—
UO2_ox1_A	2.007	4h–1600°C – Ar/O_2 5 ppm
UO2_ox1_B	2.010	4 h + 4h–1600°C – Ar/O_2 5 ppm
UO2_ox2_BQ	2.010	4 h + 4h–1600°C – Ar/O_2 5 ppm
UO2_ox2_AQ	2.010	4 h + 4h–1600°C – Ar/O_2 5 ppm, quenching at 900 °C
UO2_ox3	2.050	15h–1600°C – Ar/O_2 5 ppm
UO2_ox4	2.100	2h–850°C – Ar/O_2 100 ppm during plateau temperature

each mirror inserted before and after the DCM with a 4 mrad incidence angle. The beam size was 250 × 150 μm. The incident energy was calibrated using the absorption K-edge of potassium of a KBr pellet (3608.4 eV). HERFD-XANES was performed using the crystal-analyzer emission spectrometer in the Rowland geometry and a KETEK single-element silicon solid-state detector. The M_β emission line of U (3339 eV) was analyzed using the 220 reflection of an Si (220) bent, diced crystal analyzer with a curvature radius of 1 m. The samples were oriented at 45° with respect to the incident beam. An He-filled balloon was used to reduce the scattering of the incident and emitted X-rays by the air between the sample and the crystal analyzer and the detector. No evolution of the spectra was observed during measurements under the beam. Collected spectra were normalized using ATHENA software (Ravel and Newville, 2005). The contributions of U(IV) and U(V) were derived from the linear combination of UO_2 and U_4O_9 reference spectra.

2.3 Raman analysis

Raman spectroscopy analyses were performed on a Renishaw Invia Qontor equipped with a 1800 gr/mm grating using a He–Ne laser (633 nm). Mapping was recorded using a ×50 objective from 200 to 1300 cm^{-1}. Great care was taken to ensure that the laser did not induce any structural modification during the measurements. Starting with low to high laser powers, analyses were repeated on the same point on a pellet surface to optimize our measurement parameters and verify that Raman spectra did not change under the effect of the beam. The incident laser power was thus fixed to 0.9 mW. A silicon standard was used to calibrate the spectrometer with its line frequency fixed at 520.5 cm^{-1}. Raman mapping was performed on UO_2 pellets with a spatial resolution of 1 × 1 μm^2. Each mapping covered at least ten grains and the depth probed was estimated to be 3–5 μm (Griffiths and Hubbard, 1991). Data were processed on WIRE 5.4 software.

2.4 AFM

Atomic force microscopy (AFM) was performed on a NaioAFM microscope (Liestal, Switzerland) fitted with a 190 Al cantilever tip with the following dimensions: length, 225 μm; width, 38 μm; tip radius, 10 nm. The cantilever spring constant was 48 N m^{-1}. Data analysis was performed using Nanosurf, Naio control software in the dynamic mode. The AFM images were recorded in air and at room temperature. Data treatment was performed using Gwyddion software.

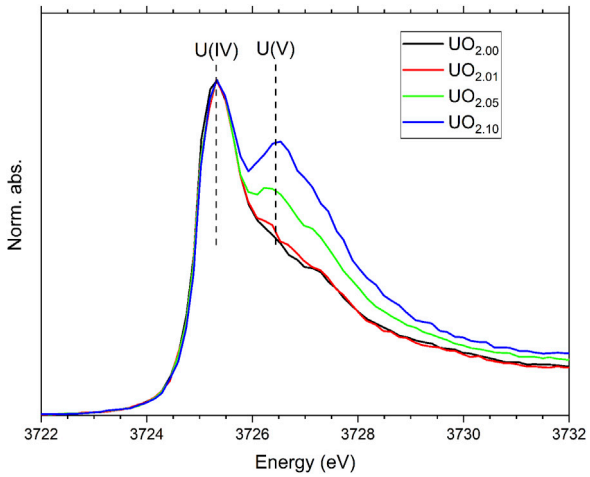

FIGURE 1
HERFD-XANES spectra at the U M_4-edge of stoichiometric UO_2 and oxidized UO_2 samples at different O/U (see Table 1 for sample details).

3 Results

3.1 Chemical state of uranium in oxidized samples

HERFD-XANES at the U M_4-edge probes the 5f unoccupied states, and it has been shown to be suitable for differentiating U(V) species from U(IV) and U(VI) (Kvashnina and Butorin, 2022). Therefore, we used this technique on UO_2 oxidized samples in order to determine the uranium oxidation state. It must be noted that at this edge, the UO_2 pellet is probed only over the first micrometer. Figure 1 displays the HERFD-XANES spectrum of a stoichiometric UO_2 compared with spectra of oxidized samples at different O/U ratios. The first peak at 3725.3 eV corresponds to U(IV), while the second peak observed at 3726.4 eV corresponds to the presence of U(V). This latter peak is thus the signature of hyper-stoichiometry.

TABLE 2 Proportion of U(IV) and U(V) and stoichiometries in UO_2 oxidized samples, obtained by linear fitting of HERFD-XANES spectra using reference compounds UO_2 and U_4O_9. The average O/U ratio was obtained by mass gain measurements after oxidation treatments.

Sample ID	Average O/U*	% UO_2	% U_4O_9	% U(IV)	% U(V)	XANES O/U ratio (±0.01) on the first µm
UO_2	2.000	100	0	100	0	2.00
UO2_ox1_B	2.010	90	10	95	5	2.02
UO2_ox3	2.050	70	30	85	15	2.08
UO2_ox4	2.100	35	65	67	33	2.16

*obtained by mass gain measurements.

UO_2 oxidation can lead to the formation of different species: UO_{2+x}, which is a mixture of U(IV) and U(V); U_4O_9 composed of 50% U(IV) and 50% U(V); U_3O_8 containing a mixture of U(V) and U(VI) (Leinders et al., 2020). We did not consider the latter oxide as we had no evidence of a U(VI) signal, which was further confirmed by Raman analysis (see below). Thus, spectra were fitted by a linear combination of U(IV) and U(V) reference spectra in order to determine the proportion between uranium oxidation degrees. Table 2 gives these results and the O/U ratio calculated from this proportion. The less oxidized sample *UO2_ox1_B* contained approximately 10% U_4O_9. Sample *UO2_ox3* contained 30% U_4O_9 and a stoichiometry at the surface which was slightly higher than the average obtained by mass gain measurements (O/U = 2.08 vs. 2.05). Analysis of the *UO2_ox4* sample showed a noticeable higher hyper-stoichiometry at the extreme surface (2.16) than average (2.10), and the presence of 65% U_4O_9.

3.2 Speciation of uranium oxide phases by Raman spectroscopy

Raman spectroscopy was used to identify the different crystallographic phases that may be present in samples after oxidation. Three phases were expected: stoichiometric UO_2, UO_{2+x}, and U_4O_9. Their respective Raman spectra are shown in Supplementary Figure S2, and Raman mappings of stoichiometric UO_2 were published in Gaillard et al. (2024). For stoichiometric UO_2, the most intense band is the T_{2g} band located at 444.6 cm^{-1}, typical of the fluorite structure. This triply degenerate mode corresponds to the symmetrical vibration of oxygen atoms around an uranium atom (Keramidas and White, 1973). The second most intense band located at ~1150 cm^{-1} corresponds to the 2LO band, an overtone of the first-order LO phonon (Livneh and Sterer, 2006; Elorrieta et al., 2018). Recent studies (Gaillard et al., 2024; Livneh, 2022) have shown that this band has a second weak contribution at 1196 cm^{-1}; we did not take this into account in this study as it does not give additional information. Indeed, this band has the same behavior as the 1196 cm^{-1} one upon the formation of U_4O_9. Bands of very weak intensities are noticeable between 500 and 700 cm^{-1}. These so-called U bands are correlated with the presence of defects in the UO_2 crystallographic structure and to the formation of domains having a local symmetry lower than that of perfect UO_2 (Guimbretière et al., 2012; Simon et al., 2023). The UO_{2+x} spectrum is similar in shape to the UO_2 spectrum. A slight blueshift of the T_{2g} band is expected as the result of the UO_2 lattice contraction (Spino and Peerani, 2008; Allen et al., 1982; He and Shoesmith, 2010). The insertion of oxygen atoms in the UO_2 fluorite structure entails the presence of defects in the material, which is seen on the Raman spectrum by a slight widening of the T_{2g} peak and an increase of the intensity of the U defect bands. Different features are observed on the U_4O_9 spectrum. A strong decrease of the T_{2g} intensity and increase of the U band intensity are observed, while the 2LO band is no longer visible. We also observe a strong width widening of the T_{2g} band, which shifts from ~445 cm^{-1} in UO_2 to ~454 cm^{-1} in U_4O_9.

TABLE 3 Summary of the T_{2g} band position and width in UO_2/UO_{2+x} and U_4O_9 phases (BQ = before quenching, AQ = after quenching, *cf.* part 2.2).

	UO_2 - UO_{2+x} phase		U_4O_9 phase	
	Position (cm^{-1})	Width (cm^{-1})	Position (cm^{-1})	Width (cm^{-1})
UO_2	444.6	15.7	-	-
U_4O_9	-	-	455	45
UO2_ox1_A	444.7	15.7	448	27
UO2_ox1_B	444.7	15.7	449	30
UO2_ox2 BQ	444.8	15.8	452	40
UO2_ox2 AQ	444.9	16.2	-	-
UO2_ox3	445.1	15.8	450	30
UO2_ox4	445.7	16.8	457	45

Thus, strong differences are present between U_4O_9 and UO_2/UO_{2+x} Raman spectra. In particular, the absence/presence of the 2LO band at 1150 cm^{-1} was used to detect the presence of U_4O_9 in the oxidized pellets. Table 3 summarizes the T_{2g} band position and width measured, respectively, in the UO_{2+x} and U_4O_9 phases of each oxidized sample.

3.2.1 UO_2 microstructure at low O/U (≤2.010)

Figure 2 presents Raman mappings of the *UO2_ox1* sample oxidized twice consecutively. The first oxidation (on the left of the figure) led to an O/U ratio of 2.007 (sample *UO2_ox1_A*), while the second oxidation (on the right of the figure) led to a 2.010 stoichiometry (sample *UO2_ox1_B*). For both O/U ratios, the same region was analyzed by Raman spectroscopy in order to study the evolution of the sample surface morphology. On the optical image (Figure 2A), the region analyzed on sample *UO2_ox1_A* is indicated with a red rectangle, while the region analyzed on sample *UO2_ox1_B* corresponds to the whole optical picture. Mappings of the 2LO band intensity are displayed in Figures

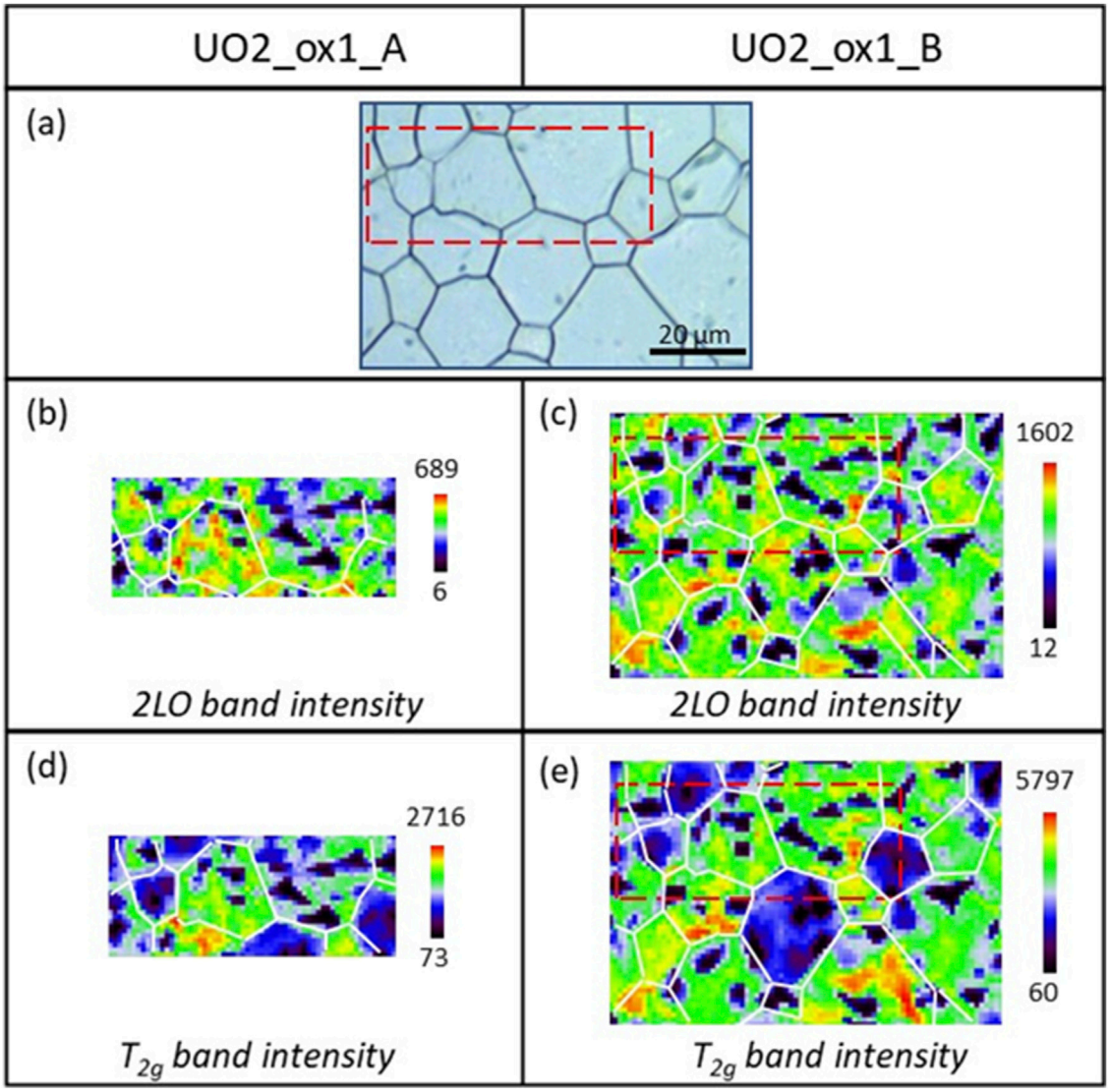

FIGURE 2
Raman mapping of the 2LO and T_{2g} band intensities at the surface of sample *UO2_ox1* after two oxidations (samples *UO2_ox1_A* on the left and *UO2_ox1_B* on the right). **(A)** Optical picture of the analyzed region; **(B)** and **(C)** Raman mapping of the 2LO band intensity; **(D)** and **(E)** Raman mapping of the T_{2g} band intensity. The color scale corresponds to the intensity scale, from the lowest (black) to the highest (red) value. For clarity, grain boundaries visible on the optical picture are represented by white lines on the mapping.

2B,C, respectively. For both samples, we observe black areas of micrometric size where the 2LO band intensity is very weak. Raman spectra extracted from one of these regions are presented in Figure 3A for both samples, corresponding to U_4O_9 species. The 2LO band is visible, although its intensity is weak, probably because the zone probed by the laser also detected a UO_{2+x} phase. In these U_4O_9 areas, the T_{2g} band position and width values (Table 3) are intermediate between those of UO_2 and U_4O_9.

Outside the U_4O_9 zones, the 2LO band intensity mapping is quite homogeneous at the surface of the samples. Raman spectra extracted from this region, on the same grain for the two samples (*UO2_ox1_A* and *UO2_ox1_B*), are presented in Figure 3B and are identical. For comparison, a spectrum of stoichiometric UO_2 is also shown in Figure 3B. We did not observe significant changes on the T_{2g} band (same position and width, see Table 3) compared to UO_2. However, the defect band intensity is noticeably higher than the stoichiometric UO_2 spectrum.

On both samples, the U_4O_9 phase forms aggregates inside grains, located heterogeneously. Note that no U_4O_9 aggregates are present in grain boundaries. Comparing the first and second oxidation, U_4O_9 aggregates have similar shapes, sizes, and locations on samples. This indicates that during the second oxidation, U_4O_9 clusters formed in the same zones than during the first oxidation. This is noticeable considering the experiment that was performed; during the second oxidation process at 1600 °C, the U_4O_9 phases formed in sample *UO2_ox1_A* dissolved and then re-crystallized during the sample cooling. Thus, U_4O_9 crystallization inside grains is not a random process but is a reversible process that occurs in defined locations inside UO_2 grains. In addition, the U_4O_9 aggregate size is comparable for both oxidations, probably because the final

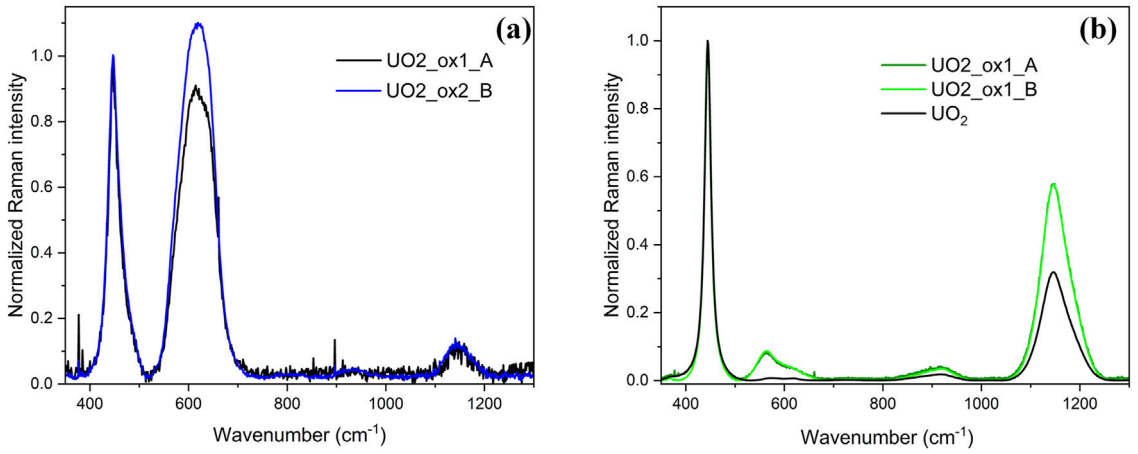

FIGURE 3
Raman spectra extracted from *UO2_ox1_A* and *UO2_ox1_B* sample mappings (*cf.* Figure 2). **(A)** Individual Raman spectra extracted in U_4O_9 area (back pixels on the mapping); **(B)** individual Raman spectra extracted in UO_{2+x} area (green pixels on the mapping). Spectra were normalized on the T_{2g} band intensity for comparison.

O/M ratios after the two oxidation treatments are close (2.007 and 2.010).

Figures 2D,E map the T_{2g} band intensity for both oxidized samples. Outside the U_4O_9 clusters, we observe that this T_{2g} intensity depends on grains. This effect is well-known and is due to the dependence of the T_{2g} intensity on the different crystalline orientations of UO_2 grains (Morgan et al., 2021; Maslova et al., 2019). Thus, the precipitation of U_4O_9 clusters inside grains does not affect global crystallography within the grain.

We performed AFM mapping on sample *UO2_ox1_B*. Particular interest was given to regions containing the U_4O_9 phase. Supplementary Figure S3A displays the Raman 2LO band intensity mapping which locates U_4O_9 zones on the pellet surface. This mapping was used to select two areas, indicated by white squares on Supplementary Figure S3A, where surface mapping was done by AFM. Supplementary Figures S3B–E show the 2D and 3D topography images. The color scale, from dark to light brown, indicates the roughness contrast at the surface. U_4O_9 zones are clearly visible as darker zones, which means that they correspond to lower planes (up to ~50 nm) than UO_2 zones. So we evidence that U_4O_9 formation entails a measurable local contraction of the lattice inside UO_2 grains, even if the lattice parameter of both oxides only differ slightly: 5.44 Å for U_4O_9 (Gronvold, 1955; Allen and Holmes, 1995; Cooper and Willis, 2004) and 5.47 Å for UO_2 (Gronvold, 1955; Desgranges et al., 2009; Leinders et al., 2015).

In conclusion, we detected the coexistence of UO_2 and U_4O_9 phases for low hyper-stoichiometric UO_2. The latter oxide crystallizes inside UO_2 grains as micrometric clusters entail a local lattice contraction without altering the overall crystallography of the grains.

3.2.2 Effect of quenching on U_4O_9 formation

Quenching is a rapid cooling process which strongly limits atomic displacements and phase transformation. It permits obtaining at room temperature crystallographic phases formed at high temperature. Therefore, quenching, instead of a slow decrease in temperature, is an effective process for overcoming the precipitation of U_4O_9 formed during heating treatment (Gronvold, 1955; Schaner, 1960; Yao et al., 2018). Sample *UO2_ox2* was first submitted to an oxidative annealing in order to obtain an O/U = 2.010. Then, it was submitted to a second thermal treatment at a temperature that entails the dissolution of the U_4O_9 phase (900°C) followed by quenching. No weight evolution of the pellet was measured before and after the quenching, indicating that the O/U ratio did not change during the experiment.

Raman spectroscopy was used to analyze the sample before and after quenching (Figure 4). Before quenching (Figures 4A,C), Raman mapping of the 2LO band intensity (Figure 4C) evidenced in black the presence of U_4O_9 clusters, as characterized previously. Interestingly, it is possible to see the shape of the U_4O_9 region on the optical picture with a weak contrast of color between U_4O_9 and UO_2 (see white circles). Figures 4B and D present the optical picture and the corresponding 2LO band intensity mapping performed in the same zone after quenching from 900 °C. We observed the disappearance of the U_4O_9 aggregates. Thus, the sample is solely composed of a $UO_{2.01}$ phase.

As observed previously for sample *UO2_ox1*, the Raman mapping exhibited two vibrational signatures, U_4O_9 and UO_{2+x}, before quenching. After quenching, only the UO_{2+x} vibrational signature is present. Figure 5 presents the average spectra of UO_{2+x} zones on the Raman mapping before (mapping without U_4O_9 areas) and after (whole mapping) quenching. Their shapes are identical except for a strong increase of defect band intensity after quenching. This can be explained by the dissolution of U_4O_9 aggregates at 900 °C and the incorporation of oxygen atoms in the UO_{2+x} lattice which increases defect concentration. This phenomenon is also visible by the slight widening of the T_{2g} band from 15.8 to 16.2 cm^{-1} and a slight but significant shift in the T_{2g} band position (*cf.* Table 3).

3.2.3 Oxidized UO_2 microstructure for O/U = 2.050

Raman mapping of the sample *UO2_ox3* is presented in Figure 6. According to mass gain measurements, this sample has an average hyper-stoichiometry of 2.05, while HERFD-XANES

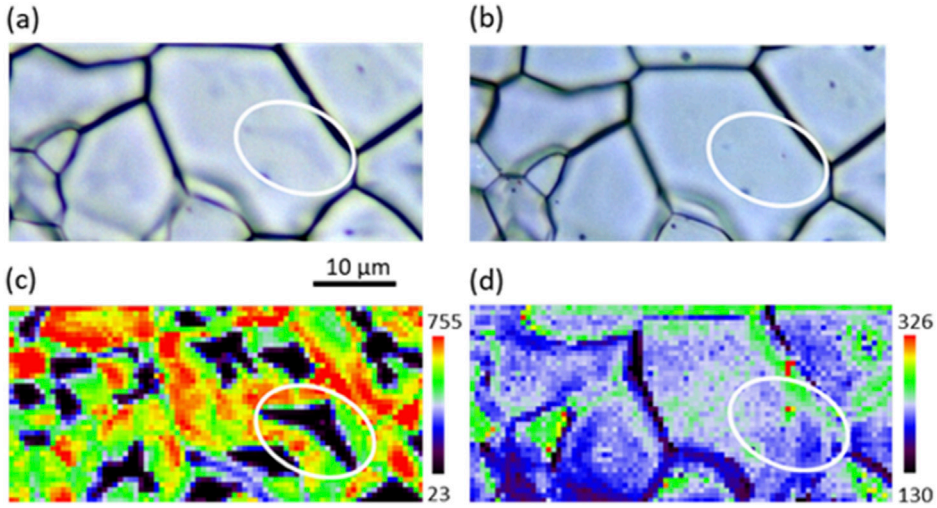

FIGURE 4
Effect of quenching on the 2LO band intensity Raman mapping of sample *UO2_ox2*. **(A)** Optical picture of the analyzed zone before and **(B)** after quenching; **(C)** and **(D)** Raman mapping of the 2LO intensity before **(C)** and after quenching **(D)**.

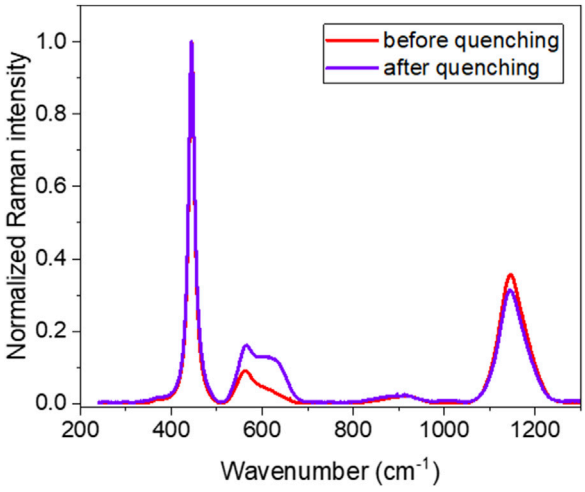

FIGURE 5
Effect of quenching on the Raman spectra of sample *UO2_ox2*. Average spectra of UO_{2+x} zones on the Raman mapping before quenching (red); average spectrum of the mapping after quenching (blue). For comparison, spectra are normalized to the T_{2g} band intensity.

analysis shows that its hyper-stoichiometry in the first micrometer is slightly higher at 2.08. This corresponds to the presence of approximately 30% of U_4O_9 in the sample, confirmed by the Raman analysis. Indeed, the 2LO band mapping intensity (Figure 6B) highlights numerous dark spots distributed over the sample surface, which correspond mainly to U_4O_9, as is shown on the Raman spectrum extracted from one of the black pixels (Supplementary Figure S4). In this sample, U_4O_9 does not form big clusters inside grains, as shown previously for lower stoichiometric samples, but is present in a rather homogeneous distribution as very small clusters inside grains (*cf.* Figure 6B). Supplementary Figure S3 also presents a spectrum extracted from a green pixel of the mapping; it is typical of a UO_{2+x} phase and exhibits a shift of the T_{2g} band to 445.1 cm^{-1}. It is interesting to note that these UO_{2+x} zones correspond mainly to grain boundaries, where little U_4O_9 is detected. Grains are slightly visible on the Raman mapping of the T_{2g} band intensity (Figure 6C). So, despite the presence of about 30% of U_4O_9, the grain crystalline orientation is somehow maintained, and the fluorite structure remains present.

3.2.4 Oxidized UO_2 microstructure for O/U = 2.10

Sample *UO2_ox4* was prepared with a final hyper-stoichiometry of 2.10, following the protocol explained in experimental Section (2.2). HERFD-XANES analysis shows that it contains approximately 65% U_4O_9 on the first micrometer, resulting in a hyper-stoichiometry of 2.16. Its Raman mapping is presented in Figure 7. The 2LO band intensity mapping displays dark areas distributed as a zebra pattern on the sample surface. We did not observe any difference between grain and grain boundaries. As shown in Figure 8, these dark areas correspond to pure U_4O_9. Elsewhere on the pellet, Raman spectra show the presence of UO_{2+x}. A spectrum extracted on a green pixel of the mapping is shown in Figure 8. A noticeable shift of the T_{2g} band position in the UO_{2+x} area measures 445.7 cm^{-1}, larger than that measured at x = 2.05. Thus, as global hyper-stoichiometry increases, the proportion of U_4O_9 and the hyper-stoichiometry of the UO_{2+x} phase increase. The T_{2g} band intensity mapping is displayed in Figure 8C. Despite the large U_4O_9 concentration, it is still possible to distinguish the contrast between grains in the UO_{2+x} phase. So, as observed at lower hyper-stoichiometries, the UO_2 lattice is maintained despite the growth of the U_4O_9 phase.

3.2.5 UO_{2+x} phase composition as a function of the sample hyper-stoichiometry

Table 3 summarizes the T_{2g} band position measured in UO_{2+x} phase of oxidized samples, and we observe that this position shifts

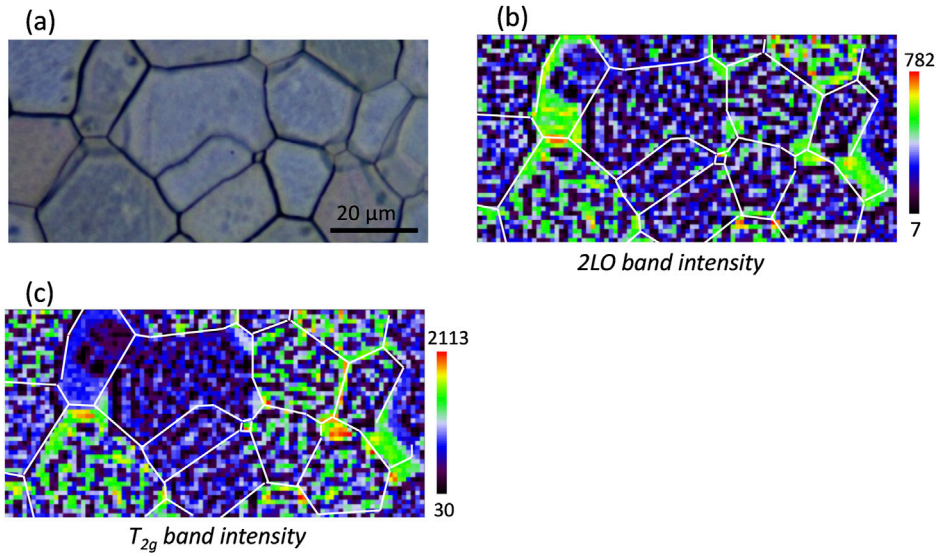

FIGURE 6
Raman mapping of sample *UO2_ox3*. **(A)** Optical picture of the analyzed zone; **(B)** 2LO band intensity mapping; **(C)** T_{2g} band intensity mapping.

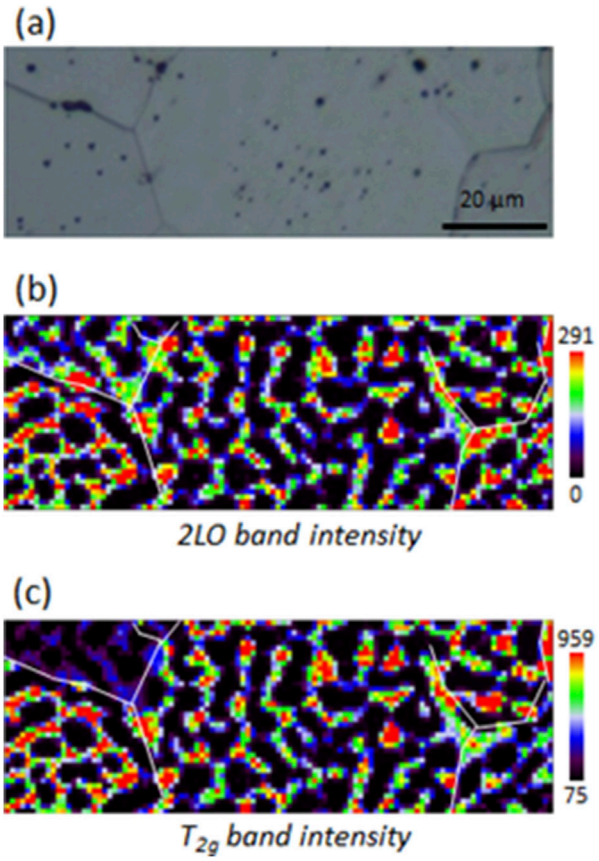

FIGURE 7
Raman mappings of sample *UO2_ox4*. **(A)** Optical picture of the analyzed zone; **(B)** 2LO band intensity mapping; **(C)** T_{2g} band intensity mapping.

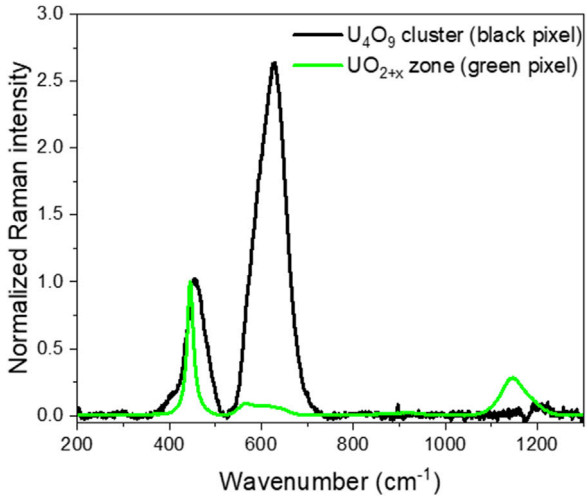

FIGURE 8
Raman spectra extracted on the mapping of sample *UO2_ox4* in U_4O_9 clusters (black pixel on the mapping) and in UO_{2+x} zone (green pixel on the mapping). Spectra are normalized to the T_{2g} band intensity.

with the global hyper-stoichiometry of samples. Thanks to these measurements, it is possible to evaluate the O/M ratio specifically in UO_{2+x} phases of our samples. Indeed, the increase of hyper-stoichiometry entails a contraction of the fluorite lattice parameter (Gronvold, 1955). This effect has a direct impact on the T_{2g} band position, which is expected to shift to higher frequencies according to the Equation 1 (McBride et al., 1994):

$$\Delta T_{2g} = -3\gamma\omega\frac{\Delta a}{a_0,} \quad (1)$$

TABLE 4 Calculation of lattice parameters A and O/U ratio in the UO_{2+x} phase of analyzed samples, from the T_{2g} band shift ΔT_{2g}. For comparison, O/U ratios obtained by mass gain are given.

	UO_{2+x} phase			Average in the sample
Sample ID	ΔT_{2g} (cm^{-1})	Calculated A (Å)	Calculated O/U	O/U from mass gain
UO2	0	5.4703	2.000	2.00
UO2_ox1_A	0.1	5.4701	2.002	2.007
UO2_ox1_B	0.1	5.4701	2.002	2.01
UO2_ox2 BQ	0.2	5.4699	2.004	2.01
UO2_ox2 AQ	0.3	5.4697	2.007	2.01
UO2_ox3	0.5	5.4693	2.010	2.05
UO2_ox4	1.1	5.4682	2.023	2.10

where γ is the Gruneisen parameter (2.17 for UO_2), ω is the T_{2g} position for stoichiometric UO_2, and Δa is the variation of the lattice parameter compared to the UO_2 one (a_0).

Therefore, knowing the T_{2g} band position shift from pristine UO_2 (ΔT_{2g}), it is possible to determine the corresponding variation of the lattice parameter (Δa) (Medyk et al., 2020), and thus to evaluate the O/M ratio in the UO_{2+x} phase. Indeed, the variation of the UO_{2+x} lattice parameter as a function of x has been widely reported in the literature (Spino and Peerani, 2008). Results are given in Table 4, where they are compared with the O/U ratio calculated for the whole pellet from mass gain after oxidative treatments. For low oxidized samples *UO2_ox1* and *UO2_ox2_BQ*, the T_{2g} band shift measured in the UO_{2+x} phase inside grains is uncertain; the corresponding O/U is actually close to 2. This means that in these samples, most additional oxygen atoms have formed the U_4O_9 phase while the UO_{2+x} phase is stoichiometric or nearly so. In sample *UO2_ox2_AQ* formed by a sole UO_{2+x} phase, the O/U value obtained by Raman measurement is in line with that obtained by mass gain measurement: ~2.01. For samples *UO2_ox3* and *UO2_ox4*, O/U ratios of the UO_{2+x} phase increase with the global hyper-stoichiometry of the samples (respectively 2.010 and 2.023) and correspond roughly to 20% of the global O/U ratio.

4 Discussion

Our study consisted of oxidizing UO_2 pellets, initially stoichiometric, to hyper-stoichiometries up to 2.1. As expected from the U–O phase diagram, we characterized two crystallographic phases, UO_{2+x} and U_4O_9, by coupling HERFD-XANES and Raman spectroscopy measurements at room temperature. A significant discrepancy is observed between the calculated O/U ratios from XANES measurements and that obtained from the mass gain of samples for the most oxidized sample at 2.1. Indeed, the hyper-stoichiometry is higher at the extreme surface of the sample (XANES probes the first micrometer) than expected. Contrary to other samples, its thermal treatment was performed at 850 °C, not at 1600 °C. At the latter, the oxygen diffusion coefficient (D) in stoichiometric polycrystalline UO_2 pellets is in the order of 10^{-6} cm^2/s (Sabioni et al., 2000). Therefore, a constant repartition of oxygen over the whole pellet depth is obtained after a 4-h annealing, and the hyper-stoichiometry can be considered as constant inside the sample. This may not be the case at 850 °C for a 3.5 h annealing. The oxygen diffusion coefficient is significantly lower at this temperature, in the order of 10^{-11}–10^{-12} cm^2/s (Sabioni et al., 2000; Dorado et al., 2011; Berthinier et al., 2013). This corresponds to a diffusion of oxygen over the first ~20 μm in sample *UO2_ox4*. However, it is known that the increase of UO_2 stoichiometry entails a significant increase of oxygen diffusion. Large discrepancies exist in the literature concerning oxygen diffusion coefficients in UO_{2+x}, probably because of the different experimental protocols used to make D measurements (Bittel et al., 1969; Bayoglu and Loreznzelli, 1984; Lay, 1970; Ruello et al., 2004). According to those data, the oxygen diffusion coefficient may range from 10^{-8} to 10^{-13} cm^2/s at 850 °C. Therefore, it is difficult to precisely evaluate the diffusion depth of oxygen in sample *UO2_ox4*. It is expected to be above 20 μm but may not be large enough to assure a constant repartition of oxygen over the whole depth. This question will be addressed in further research by the characterization of pellet cross-sections.

Some have noticed preferential oxidation as a function of the grain orientation, based on work on UO_2 single-crystals (Allen et al., 1988a; Allen et al., 1988b). We did not observe this phenomenon, as the amount of U_4O_9 was homogeneous at the pellet surface whatever the O/U. However, the experimental conditions used by Allen (300 °C, 1 torr of O_2) significantly differ from ours and led to the formation of upper oxides (U_3O_7 and U_3O_8) not observed in our work. This also highlights the effect of the oxidative conditions on the nature of the oxides formed. In our study, oxidative annealing treatments were performed at 1600 °C or 850 °C—temperatures where the sole existing phase is UO_{2+x}. The crystallographic phases we further characterized at room temperature are those "allowed" to form during the sample cooling—UO_{2+x} and U_4O_9 according to the U–O phase diagram. When oxidation treatments are performed at lower temperature and under stronger oxidative conditions such as air, a prompt conversion of U_4O_9 into U_3O_7 and eventually U_3O_8 is observed (De Bona et al., 2022; Milena-Perez et al., 2023; Teixeira and Imakuma, 1991).

Thanks to the analysis of Raman mapping, we could evaluate the composition of the UO_{2+x} phases as a function of the global O/U ratio of samples, while XANES could help evaluate the proportion of U_4O_9 inside samples. At low O/U (~0.01), the UO_{2+x} phase can be considered stoichiometric, which means that samples are composed of UO_2 and ~10% of U_4O_9. For O/U ≥ 2.05, samples are composed of U_4O_9 and of a UO_{2+x} phase whose hyper-stoichiometry increases with the global O/U ratio. For O/U = 2.05, samples are composed of ~70% of $UO_{2.01}$ and ~30% of U_4O_9, while at O/U = 2.1, they are composed of ~65% U_4O_9 and 35% $UO_{2.02}$. We thus observe that UO_{2+x} phases display quite low O/M ratios, even for high global hyper-stoichiometries.

We could detect the U_4O_9 growth mechanism inside grains. At low hyper-stoichiometry (2.01), U_4O_9 is present as micrometric clusters inside stoichiometric UO_2 grains. These clusters were formed during the slow cooling of our sample from a homogeneous UO_{2+x} phase. Such clusters were evidenced by Allen et al. (1983) but for highly oxidized UO_2 pellets at O/U = 2.24. As the hyper-stoichiometry increases to O/U = 2.1, these clusters coalesce to form a U_4O_9 network at the surface of the material. This kind of microstructure can be compared to those reported by previous research, showing that the precipitation of U_4O_9 in UO_{2+x} leads to a Widmanstätten needle structure or the formation of platelets (Tuxworth and Evans, 1959) (Lierde et al., 1970; Whillock and Pearce, 1990; Schaner, 1960). The formation of U_4O_9 entails a local lattice contraction inside grains, evidenced by AFM, but without affecting the surrounding UO_2 matrix. Even for high hyper-stoichiometry (x > 2.1) where U_4O_9 is the main crystallographic phase, the UO_2 lattice is preserved and, consequently, we always observe a joint presence of two crystallographic phases. This is comparable with observations made by Allen et al. (1983) on UO_2 pellets and Leinders et al. (2016) on UO_2 nanopowders. We also show by twice oxidizing a UO_2 sample at high temperature (1600 °C) that U_4O_9 clustering inside UO_2 grains is not a random process and that it occurs in defined zones inside grains. One may link this fact with the presence of defects in grains that may constitute nucleation sites. The precipitation of U_4O_9 in UO_{2+x} occurs by the agglomeration of oxygen atoms that produces defects. For this reason, some authors consider that the interface between UO_{2+x} and U_4O_9 is equivalent to dislocations (Chevrel, 1992). One may envision that after the re-dissolution of U_4O_9, dislocations remain and, during the second oxidation annealing, favor the recrystallization of U_4O_9 in the same zone of grains. We have also observed that the formation of U_4O_9 occurs only inside grains, not in grain boundaries. The latter contain a high concentration of defects like dislocations that entail a lower crystallinity and, probably, tensile strains that may entail the clustering of U_4O_9.

5 Conclusion

We studied the UO_{2+x}/U_4O_9 phase equilibrium in UO_2 in the hyper-stoichiometry range $0.01 < x < 0.1$ after thermal oxidation treatments performed under dry conditions at 850 °C or 1600 °C. By coupling HERFD-XANES at the uranium M_4-edge and micro-Raman spectroscopy mapping, we could determine the proportion between each phase and their composition.

At low O/U, U_4O_9 is present as small clusters inside UO_2 grains. Their formation, occurring during the slow cooling of our samples, does not occur in a random area of grains. Indeed, we show by twice repeating the annealing/cooling process that the U_4O_9 cluster size and location are identical. The presence of U_4O_9 entails a local contraction of the lattice, measurable by AFM, which does not affect the global structure of grains, even at a high U_4O_9 concentration.

As the O/U increases, the proportion of U_4O_9 and the UO_{2+x} phase hyper-stoichiometry increase, leading to the formation of a network of U_4O_9 crystallized inside UO_{2+x} grains. However, even for highly oxidized samples, we observed that the UO_{2+x} phases exhibit only a slight O/M, meaning that during the slow cooling process, most of the additional oxygen atoms are incorporated as U_4O_9 in the samples.

Data availability statement

The raw data supporting the conclusions of this article will be made available by the authors, without undue reservation.

Author contributions

CG: conceptualization, formal analysis, funding acquisition, investigation, project administration, supervision, and writing–original draft. HL: formal analysis, investigation, and writing–original draft. LS: formal analysis, investigation, and writing–original draft. YP: funding acquisition and writing–review and editing. RD: funding acquisition and writing–review and editing. NM: funding acquisition and writing–review and editing.

Funding

The authors declare that financial support was received for the research, authorship, and/or publication of this article. The authors acknowledge the support of the French Agence Nationale de la Recherche (ANR) under grant ANR-21-CE05-0035 (project BENEFICIA).

Acknowledgments

We acknowledge S. Forel (LMI, UCBL, France) for her assistance using AFM, and M. Pijolat, V. Péres, and L. Vieille (Mines St Etienne, France) for the TGA experiments. The authors would also like to thank R. Fillol (IP2I) for his helpful technical contribution. We acknowledge SOLEIL for the provision of synchrotron radiation facilities, and we would like to thank M. Hunault and P-L. Solari for assistance in using beamline MARS.

Conflict of interest

The authors declare that the research was conducted in the absence of any commercial or financial relationships that could be construed as a potential conflict of interest.

Publisher's note

All claims expressed in this article are solely those of the authors and do not necessarily represent those of their affiliated organizations, or those of the publisher, the editors, and the reviewers. Any product that may be evaluated in this article, or claim that may be made by its manufacturer, is not guaranteed or endorsed by the publisher.

Supplementary material

The Supplementary Material for this article can be found online at: https://www.frontiersin.org/articles/10.3389/fnuen.2024.1465080/full#supplementary-material

References

Allen, G. C., Buswell, J. T., and Tempest, P. A. (1983). Ordering phenomena in U_4O_{9-y} crystals studied by Transmission electron Microscopy. *J. Chem. Soc. Dalton Trans.*, 589–590. doi:10.1039/dt9830000589

Allen, G. C., and Holmes, N. R. (1995). A mechanism for the UO_2 to α-U_3O_8 phase transformation. *J. Nucl. Mater.* 223, 231–237. doi:10.1016/0022-3115(95)00025-9

Allen, G. C., Tempest, P. A., and Tyler, J. W. (1982). Coordination model for the defect structure of hyperstoichiometric UO_{2+x} and U_4O_9. *Nature* 295, 48–49. doi:10.1038/295048a0

Allen, G. C., Tempest, P. A., and Tyler, J. W. (1988a). Characterisation of crystalline UO_2 oxidised in 1 torr of oxygen at 25, 225 and 300°C; Part 1. X-Ray Photoelectron Spectroscopy. *J. Chem. Soc. Faraday Trans.* 84, 4049. doi:10.1039/f19888404049

Allen, G. C., Tempest, P. A., and Tyler, J. W. (1988b). Characterization of crystalline UO_2 oxidized in 1 Torr of oxygen at 25, 225 and 300°C; Part 2. X-ray diffraction and Scanning electron Microscopy. *J. Chem. Soc. Faraday Trans.* 84, 4061. doi:10.1039/f19888404061

Bannister, M. J., and Buykx, W. J. (1974). A dilatometric study of the solubility of U_4O_9 in UO_2. *J. Nucl. Mater.* 55, 345–351. doi:10.1016/0022-3115(75)90075-6

Bayoglu, A. S., and Loreznzelli, R. (1984). Oxygen diffusion in fcc fluorite type nonstoichiometric nuclear oxides $MO_{2+/-x}$. *Sol. State Ion.* 12, 53–66. doi:10.1016/0167-2738(84)90130-9

Berthinier, C., Rado, C., Chatillon, C., and Hodaj, F. (2013). Thermodynamic assessment of oxygen diffusion in non-stoichiometric $UO_{2+/-x}$ from experimental data and Frenkel pair modeling. *J. Nucl. Mater.* 433, 265–286. doi:10.1016/j.jnucmat.2012.09.011

Bittel, J. T., Sjodahi, I. H., and White, J. F. (1969). Steam oxidation kinetics and oxygen diffusion in UO2 at high temperatures. *J. Am. Ceram. Soc.* 52, 446. doi:10.1111/j.1151-2916.1969.tb11976.x

Blackburn, P. E. (1958). Oxygen dissociation pressures over uranium oxides. *J. Phys. Chem.* 62, 897–902. doi:10.1021/j150566a001

Chevrel, H., Frlttage à basse temperature du dioxyde d'uranium, en conditions de sur-stoechiometrie temporaire, Rapport CEA R-5569, (1992).

Cooper, R. I., and Willis, B. T. M. (2004). Refinement of the structure of β-U_4O_9. *Acta Crystallogr. Sect. A* 60, 322–325. doi:10.1107/s010876730401219x

De Bona, E., Popa, K., Walter, O., Cologna, M., Hennig, C., Scheinost, A. C., et al. (2022). Oxidation of micro- and nanograined UO_2 pellets by *in situ* synchrotron X-ray diffraction. *Inorg. Chem.* 61, 1843–1850. doi:10.1021/acs.inorgchem.1c02652

Desgranges, L., Baldinozzi, G., Rousseau, G., Nièpce, J. C., and Calvarin, G. (2009). Neutron diffraction study of the *in situ* oxidation of UO_2. *Inorg. Chem.* 48, 7585–7592. doi:10.1021/ic9000889

Desgranges, L., Baldinozzi, G., Siméone, D., and Fischer, H. E. (2011). Refinement of the α-U_4O_9 crystalline structure: new insight into the U_4O_9 -> U_3O_8 transformation. *Inorg. Chem.* 50, 6146–6151. doi:10.1021/ic200316b

Dorado, B., Garcia, P., Carlot, G., Fraczkiewicz, M., Pasquet, B., Freyss, M., et al. (2011). First-principles calculation and experimental study of oxygen diffusion in uranium dioxide. *Phys. Rev. B* 83, 035126. doi:10.1103/physrevb.83.035126

Elorrieta, J. M., Bonales, L. J., Baonza, V. G., and Cobos, J. (2018). Temperature dependence of the Raman spectrum of UO_2. *J. Nucl. Mater.* 503, 191–194. doi:10.1016/j.jnucmat.2018.03.015

Gaillard, C., Sarrasin, L., Panetier, C., Pipon, Y., Ducher, R., and Moncoffre, N. (2024). Isotopic effect of oxygen on the Raman mapping of a polycrystalline uranium dioxide UO_2. *J. Raman Spectrosc.* 55, 678–687. doi:10.1002/jrs.6660

Garrido, F., Nowicki, L., and Thomé, L. (2006). Channeling investigation of the crystalline structure of U_4O_{9-y}. *Phys. Rev. B* 74, 184114. doi:10.1103/physrevb.74.184114

Griffiths, T. R., and Hubbard, H. V.St.A. (1991). Absorption spectrum of single-crystal UO_2: identification of and effect of temperature on the peak positions of essentially all optical transitions in the visible to near infrared regions using derivative spectroscopy. *J. Nucl. Mater.* 185, 243–259. doi:10.1016/0022-3115(91)90510-e

Gronvold, F. (1955). High-temperature X-ray study of uranium oxides in the UO_2 - U_3O_8 region. *J. Inorg. Nucl. Chem.* 1, 357–370. doi:10.1016/0022-1902(55)80046-2

Guéneau, C., Baichi, M., Labroche, D., Chatillon, C., and Sundman, B. (2002). Thermodynamic assessment of the uranium-oxygen system. *J. Nucl. Mater.* 304, 161–175. doi:10.1016/s0022-3115(02)00878-4

Guimbretière, G., Desgranges, L., Canizarès, A., Carlot, G., Caraballo, R., Jégou, C., et al. (2012). Determination of in-depth damaged profile by Raman line scan in a pre-cut He^{2+} irradiated UO_2. *Appl. Phys. Lett.* 100, 251914. doi:10.1063/1.4729588

He, H., and Shoesmith, D. (2010). Raman spectroscopic studies of defect structures and phase transition in hyper-stoichiometric UO_{2+x}. *Phys. Chem. Chem. Phys.* 12, 8108. doi:10.1039/b925495a

Higgs, J. D., Thompson, W. T., Lewis, B. J., and Vogel, S. C. (2007). Kinetics of precipitation of U_4O_9 from hyperstoichiomectric UO_{2+x}. *J. Nucl. Mater.* 366, 297–305. doi:10.1016/j.jnucmat.2007.03.054

Horlait, D., Domange, J., Amany, M.-L., Gérardin, M., Barthe, M.-F., Carlot, G., et al. (2023). Experimental investigation of Kr diffusion in UO_{2+x}: slight deviations from stoichiometry, significant effects on diffusion kinetics and mechanisms. *J. Nucl. Mater.* 574, 154191. doi:10.1016/j.jnucmat.2022.154191

Ishii, T., Naito, K., and Oshima, K. (1970). X-ray study on a phase transition and a phase diagram on the U_4O_9 phase. *Solid State Commun.* 8, 677–683. doi:10.1016/0038-1098(70)90194-8

Keramidas, V. G., and White, W. B. (1973). Raman spectra of oxides with the fluorite structure. *J. Chem. Phys.* 59, 1561–1562. doi:10.1063/1.1680227

Kudo, T., Kida, M., Nakamura, T., Nagase, F., and Fuketa, T. (2007). Effects of fuel oxidation and dissolution on volatile fission product release under severe accident conditions. *J. Nucl. Sci. Technol.* 44, 1428–1435. doi:10.1080/18811248.2007.9711390

Kvashnina, K. O., and Butorin, S. M. (2022). High-energy resolution X-ray spectroscopy at actinide $M_{4,5}$ and ligand K edges: what we know, what we want to know, and what we can know. *Chem. Comm.* 58, 327–342. doi:10.1039/d1cc04851a

Lay, K. W. (1970). Oxygen chemical diffusion coefficient of uranium dioxide. *J. Am. Ceram. Soc.* 53, 369–373. doi:10.1111/j.1151-2916.1970.tb12134.x

Le Gall, C., Audubert, F., Lechelle, J., Pontillon, Y., and Hazemann, J.-L. (2020). Contribution to the study of fission products release from nuclear fuels in severe accident conditions: effect of the pO_2 on Cs, Mo and Ba speciation, EPJ Nuclear. *Sci. Technol.* 6, 2. doi:10.1051/epjn/2019058

Leinders, G., Bes, R., Kvashnina, K. O., and Verwerft, M. (2020). Local structure in U(IV) and U(V) environments: the case of U_3O_7. *Inorg. Chem.* 59, 4576–4587. doi:10.1021/acs.inorgchem.9b03702

Leinders, G., Cardinaels, T., Binnemans, K., and Verwerft, M. (2015). Accurate lattice parameter measurements of stoichiometric uranium dioxide. *J. Nucl. Mater.* 459, 135–142. doi:10.1016/j.jnucmat.2015.01.029

Leinders, G., Pakarinen, J., Delville, T., Binnemans, K., and Verwerft, M. (2016). Low-temperature oxidation of fine UO_2 powders: a process of nanosized domain development. *Inorg. Chem.* 55, 3915–3927. doi:10.1021/acs.inorgchem.6b00127

Lierde, W. V., Pelsmaekers, J., and Lecocq-Robert, A. (1970). On the phase limits of U_4O_9. *J. Nucl. Mater.* 37, 276. doi:10.1016/0022-3115(70)90157-1

Lindemer, T. B., and Besmann, T. M. (1985). Chemical thermodynamic representation of $UO_{2+/-x}$. *J. Nucl. Mater.* 130, 473–488. doi:10.1016/0022-3115(85)90334-4

Livneh, T. (2022). Resonant Raman scattering in UO_2 revisited. *Phys. Rev. B* 105, 045115. doi:10.1103/physrevb.105.045115

Livneh, T., and Sterer, E. (2006). Effect of pressure on the resonant multiphonon Raman scattering in UO_2. *Phys. Rev. B* 73, 085118. doi:10.1103/physrevb.73.085118

Maslova, O. A., Iltis, X., Desgranges, L., Ammar, M. R., Genevois, C., Bilbao, E. d., et al. (2019). Characterization of an UO_2 ceramic via Raman imaging and electron backscattering diffraction. *Mater. Charact.* 147, 280–285. doi:10.1016/j.matchar.2018.11.006

Matsui, T., and Naito, K. (1975). Phase relation and defect structures of nonstoichiometric $U_4O_{9+/-y}$ and UO_{2+x} at high temperature. *J. Nucl. Mater.* 56, 327. doi:10.1016/0022-3115(75)90050-1

McBride, J. R., Hass, K. C., Poindexter, B. D., Weber, W. H., Pr, Nd, Eu, Gd, et al. (1994). Raman and x-ray studies of Ce1−*x*RE*x*O2−*y*, where RE=La, Pr, Nd, Eu, Gd, and Tb. *Appl. Phys.* 76, 2435–2441. doi:10.1063/1.357593

Mc Eachern, R. J. (1997). A review of kinetic data on the rate of U_3O_7 formation on UO_2. *J. Nucl. Mater.* 245, 238. doi:10.1016/S0022-3115(96)00733-7

Mc Eachern, R. J., and Taylor, P. (1998). A review of the oxidation of uranium dioxide at temperatures below 400°C. *J. Nucl. Mater.* 254, 87. doi:10.1016/S0022-3115(97)00343-7

Medyk, L., Manara, D., Colle, J. Y., Bouexière, D., Vigier, J.-F., Marchetti, L., et al. (2020). Determination of the plutonium content and O/M ratio of (U,Pu)O 2-x using Raman spectroscopy. *J. Nucl. Mater.* 541, 152439. doi:10.1016/j.jnucmat.2020.152439

Milena-Perez, A., Rodriguez-Villagra, N., Fernandez-Carretero, S., and Nunez, A., Thermal air oxidation of UO_2: joint effect of precursor's nature and particle size distribution, *Prog. Nucl. Ener.*, 159 (2023) 104629. doi:10.1016/j.pnucene.2023.104629

Morgan, P. K., Prusnick, T. A., Velez, M. A., Rickert, K., Turner, D. B., and Mann, J. M. (2021). Identifying crystallographic faces of the fluorites urania and thoria with rotational polarized Raman spectroscopy. *J. Raman Spectrosc.* 52, 1902–1909. doi:10.1002/jrs.6236

Ravel, B., and Newville, M. (2005). ATHENA, ARTEMIS, HEPHAESTUS: data analysis for X-ray absorption spectroscopy using IFEFFIT. *J. Synchrotron Rad.* 12, 537–541. doi:10.1107/s0909049505012719

Rousseau, G., Desgranges, L., Charlot, F., Millot, N., Nièpce, J. C., Pijolat, M., et al. (2006). A detailed study of UO_2 to U_3O_8 oxidation phases and the associated rate-limiting steps. *J. Nucl. Mater.* 355, 10–20. doi:10.1016/j.jnucmat.2006.03.015

Ruello, P., Chirlesan, G., Petot-Ervas, G., Petot, C., and Desgranges, L. (2004). Chemical diffusion in uranium dioxide - influence of defect interactions. *J. Nucl. Mater.* 325, 202–209. doi:10.1016/j.jnucmat.2003.12.007

Sabioni, A. C. S., Ferraz, W. B., and Millot, F. (2000). Effect of grain boundaries on uranium and oxygen diffusion in polycrystalline UO_2. *J. Nucl. Mater.* 278, 364–369. doi:10.1016/s0022-3115(99)00250-0

Schaner, B. E. (1960). Metallographic determination of the UO_2-U_4O_9 phase diagram. *J. Nucl. Mater.* 2, 110–120. doi:10.1016/0022-3115(60)90038-6

Simon, P., Canizarès, A., Raimboux, N., and Desgranges, L. (2023). How can Raman spectroscopy be used to study nuclear fuel? *MRS Bull.* 48, 118–123. doi:10.1557/s43577-022-00371-w

Sitaud, B., Solari, P. L., Schlutig, S., Llorens, I., and Hermange, H. (2012). Characterization of radioactive materials using the MARS beamline at the synchrotron SOLEIL. *J. Nucl. Mater.* 425, 238–243. doi:10.1016/j.jnucmat.2011.08.017

Soulié, A., Baldinozzi, G., Garrido, F., and Crocombette, J.-P. (2019). Clusters of oxygen interstitials in UO_{2+x} and α-U_4O_9: structure and arrangements. *Inorg. Chem.* 58, 12678–12688. doi:10.1021/acs.inorgchem.9b01483

Spino, J., and Peerani, P. (2008). Oxygen stoichiometry shift of irradiated LWR-fuels at high burn-ups: review of data and alternative interpretation of recently published results. *J. Nucl. Mater.* 375, 8–25. doi:10.1016/j.jnucmat.2007.10.007

Taylor, P. (2005). Thermodynamic and kinetic aspects of UO_2 fuel oxidation in air at 400-2000 K. *J. Nucl. Mater.* 344, 206–212. doi:10.1016/j.jnucmat.2005.04.043

Teixeira, S. R., and Imakuma, K. (1991). High temperature X-ray diffraction study of the U_4O_9 formation on UO_2 sintered plates. *J. Nucl. Mater.* 178, 33–39. doi:10.1016/0022-3115(91)90453-e

Tuxworth, R. H., and Evans, W. (1959). Habit planes for U_4O_9 precipitation in uranium dioxide. *J. Nucl. Mater.* 3, 302–303. doi:10.1016/0022-3115(59)90027-3

Whillock, S., and Pearce, J. H. (1990). A method of determining the distribution of U_4O_9 in oxidised UO_2. *J. Nucl. Mater.* 175, 121–128. doi:10.1016/0022-3115(90)90278-u

Yao, T., Scott, S. M., Xin, G., Gong, B., and Lian, J. (2018). Dense nanocrystalline UO_{2+x} fuel pellets synthetized by high pressure spark plasma sintering. *J. Am. Ceram. Soc.* 101, 1105–1115. doi:10.1111/jace.15289